PHYSICAL REVIEW D **86,** 055022 (2012)

# Supersymmetry with prejudice: Fitting the wrong model to LHC data

B. C. Allanach[1,*] and Matthew J. Dolan[2,†]

[1]*Department of Applied Mathematics and Theoretical Physics, Centre for Mathematical Sciences, University of Cambridge, Wilberforce Road, Cambridge CB30WA, United Kingdom*

[2]*Institute for Particle Physics Phenomenology, Department of Physics, University of Durham, Science Laboratories, South Road, Durham DH13LE, United Kingdom*

(Received 12 September 2011; revised manuscript received 4 April 2012; published 18 September 2012)

We critically examine interpretations of hypothetical supersymmetric LHC signals, fitting to alternative wrong models of supersymmetry breaking. The signals we consider are some of the most constraining on the sparticle spectrum: invariant mass distributions with edges and endpoints from the golden decay chain $\tilde{q} \to q\chi_2^0(\to \tilde{l}^{\pm} l^{\mp} q) \to \chi_1^0 l^+ l^- q$. We assume a constrained minimal supersymmetric standard model (CMSSM) point to be the 'correct' one, but fit the signals instead with minimal gauge mediated supersymmetry breaking models (mGMSB) with a neutralino quasistable lightest supersymmetric particle, minimal anomaly mediation and large volume string compactification models. Minimal anomaly mediation and large volume scenario can be unambiguously discriminated against the CMSSM for the assumed signal and 1 fb$^{-1}$ of LHC data at $\sqrt{s} = 14$ TeV. However, mGMSB would not be discriminated on the basis of the kinematic endpoints alone. The best-fit point spectra of mGMSB and CMSSM look remarkably similar, making experimental discrimination at the LHC based on the edges or Higgs properties difficult. However, using rate information for the golden chain should provide the additional separation required.

DOI: 10.1103/PhysRevD.86.055022 PACS numbers: 12.60.Jv, 14.80.Ly

## I. INTRODUCTION

The Large Hadron Collider (LHC) is currently actively engaged in searches for new physics, including supersymmetry (SUSY). No signal has yet been found, and the CMS and ATLAS experiments have significantly extended previous exclusion limits [1,2]. In the near future, as more data are collected by the experiments, the observation of a supersymmetric signal is quite plausible. In the event of a signal, it will be important to extract as much empirical information as possible about the sparticle spectrum, since it contains clues about the mechanism of supersymmetry breaking. We may hope to rule out one mechanism in favor of another. One will want to bring all of the data that robustly constrain the supersymmetry breaking mechanism to bear in order to separate different models empirically. However, the usual search variables (number of events past certain cuts or total cross sections), while perfectly suited to searching for supersymmetry, are blunt instruments when it comes to measuring supersymmetric masses in detail: they give only gross information about the overall mass scale of the supersymmetric particles. Since this is typically described by some parameter in the SUSY breaking mechanism, such measurements will not tend to be very good at disentangling models. One needs to measure observables which are sensitive to the mass spectrum of the sparticles, reasonably accurate, and robust with respect to experimental systematics such as how well one has parametrized one's detector. Arguably the best examples of such observables come from SUSY cascade decays. SUSY cascade decay chains give specific kinematics to the final state particles, and particular kinematic variables have been shown to contain a wealth of information about the sparticle masses. Maxima and minima of invariant mass distributions, if observed, have several advantages in the inference of sparticle masses. They can be essentially Standard Model background free, particularly if flavor subtracted. Also, although the shape [3] of the distributions themselves is subject to significant detector corrections, which may require a lot of integrated luminosity to model well, the endpoints of the distributions are expected to be much less sensitive to such effects. For example, the golden decay chain

$$\tilde{q} \to q\chi_2^0(\to \tilde{l}^{\pm} l^{\mp} q) \to \chi_1^0 l^+ l^- q, \tag{1.1}$$

shown in Fig. 1 has been shown to be most useful [4]. The presence of this cascade leads to events with two opposite-sign same-flavor leptons, jets and missing energy. The endpoints yield useful information coming from the

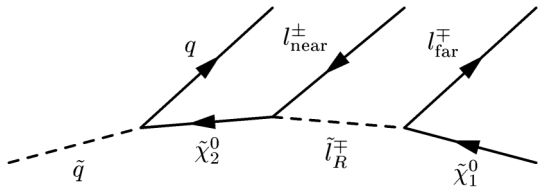


FIG. 1. The golden decay chain $\tilde{q} \to \chi_2^0 q(\to \tilde{l}^{\pm} l^{\mp} q) \to \chi_1^0 l^+ l^- q$.

*B.C.Allanach@damtp.cam.ac.uk
†m.j.dolan@durham.ac.uk

 

invariant mass distributions of the dileptons $m_{ll}$, from the jet and lepton pair $m_{llq}$ and from each lepton and the jet $m_{lq}$. Despite the fact that one obtains highly correlated mass measurements from such endpoints, considering the measurements in parallel helps discriminating different models of supersymmetry breaking [5]. Even if additional decay chains are identified in the data, they are not expected to add significant discriminatory power over the dominant golden chain. It is by no means guaranteed that the golden decay chain is present, however. For instance, it only exists in about a quarter of the parameter space [6] of the constrained minimal supersymmetric standard model (CMSSM). In the case that the golden chain is not present, one would use kinematic edge data from all chains that one can identify. The resulting information is then likely to be less constraining on the sparticle spectrum than the golden chain. We then view studies assuming the observation of the golden decay chain to be the most optimistic cases as far as model discrimination goes. If two models cannot be experimentally discriminated with this assumption, it is extremely unlikely that they will be discriminated between without the golden cascade. The kinematic data have been further combined with cross-section information in order to improve the precision of mass measurements within particular models with more parameters than the CMSSM [7].

Combining the power of the LHC and a linear collider leads to much more information about the model than is possible from LHC measured kinematic endpoints, and constitutes a significant improvement on the information obtained from the LHC alone [8]. Using SUSY signal measurements from both a linear collider and the LHC in order to measure a large part of the minimal supersymmetric standard model (MSSM) spectrum may be possible, allowing checks of unification relations in various models [9–11]. The additional information coming from linear collider data would be ideal to include in order to discriminate models, but in this paper we restrict ourselves to potential LHC data, since the linear collider is not yet built.

Kinematic edge predictions resulting from golden chain decays have been examined in the literature to see if there could be model discrimination coming from their measurement. In Ref. [12], it was seen whether the ratios of the measurements would discriminate the CMSSM, an intermediate-scale string model and a mirage unification model. The parameters of the models were all scanned over, but no experimental errors were taken into account. In any case, it was concluded that there was no clear separation between the models from using the edge variables, even for infinitely precise measurements. We go beyond this work by examining different models, and by fixing a benchmark model such that we can use the experimental resolutions estimated by ATLAS, assuming a certain integrated luminosity. In Ref. [13], the golden decay chain was used in fits to the CMSSM. Hypothetical invariant mass endpoints were fit using different sparticle spectrum calculators in order to examine the differences between them, quantifying the theoretical error. The best-fit values of each spectrum calculator were within 95% confidence level limits of each other, assuming a huge LHC luminosity (300 $\text{fb}^{-1}$). A number of other fitting groups have investigated the effects of LHC data on global fits to the CMSSM, including the Fittino Collaboration [14], SFitter [15] and Refs. [16,17]. Those works focused more on the constraining power of the LHC data on CMSSM fits. In Ref. [18], current indirect data on $B$ decays, electroweak observables and the dark matter relic density were combined with direct sparticle search limits in fits to the CMSSM, minimal anomaly mediation (mAMSB), large volume scenario (LVS) and minimal gauge mediated supersymmetry breaking (mGMSB) models (to be introduced below) in order to examine whether current data show any preference for the model of supersymmetry breaking. It was found that current indirect data are too weak to select any of the models. On the other hand, endpoint data taken from the golden cascade would be enough to robustly constrain the CMSSM in 1 $\text{fb}^{-1}$ of integrated luminosity, at a particular benchmark point studied by ATLAS, called SU3 [16]. Such robustness is signaled by prior independence in Bayesian fits, indicating that the data are sufficiently powerful to constrain the model hypothesized. Reference [19] also examined fits from the SU3 point golden cascade fits on the CMSSM (with and without including cosmological data) as well as models with more free parameters than the CMSSM. Model comparison between the nonuniversal Higgs model, the CMSSM and the CMSSM but with nonuniversal gaugino masses was examined using Bayesian techniques. Some nonrobustness in the non-CMSSM models with respect to changing the priors was discovered: there was not enough power in the data to properly constrain the models with larger parameter spaces.

Since the CMSSM may be robustly constrained by the endpoint data, but models with more parameters may not, in the present paper we answer the following question: is kinematic edge data from 1 $\text{fb}^{-1}$ of the 14 TeV LHC constraining enough to allow us to distinguish between simpler different models of supersymmetry breaking (i.e., with fewer parameters in the CMSSM)? This question will require a numerical statistical analysis. Even if it is clear analytically that a model can be chosen such that its mass spectrum is close to the CMSSM, the question is: can it be made close *enough* in terms of the errors on the observables to provide a viable fit? Conversely, even if two models cannot exactly reproduce the same mass spectrum, are the errors on the observables small enough such that the two models are discriminated? We shall test robustness by looking for a *lack* of prior dependence in the hypothesis testing, and agreement between Bayesian and frequentist inferences.

## II. SUSY BREAKING MODELS

In this section, we summarize the alternative hypotheses of SUSY breaking that we shall use. The parameters of the CMSSM are a flavor blind SUSY breaking scalar mass $m_0$, a common gaugino mass $M_{1/2}$, a flavor blind SUSY breaking scalar trilinear coupling $A_0$ and $\tan\beta$, the ratio of the MSSM Higgs vacuum expectation values. Below a grand unification theory (GUT) scale of $M_{\rm GUT} \sim 2 \times 10^{16}$ GeV, the SUSY breaking terms of different flavors evolve separately to the weak scale. In anomaly mediated SUSY breaking [20], SUSY breaking is communicated to the visible sector via the super-Weyl anomaly. In its original manifestation, pure anomaly mediation suffers from negative slepton mass squared parameters, signaling a scalar potential minimum inconsistent with a massless photon. mAMSB assumes the existence of an additional contribution to scalar masses $m_0$ at $M_{\rm GUT}$ giving it a total of three parameters: the vacuum expectation value of the auxiliary field in the supergravity multiplet representing the overall sparticle mass scale, $m_{\rm aux}$, $m_0$ and $\tan\beta$. As advertised above, mGMSB [21] also has three continuous parameters: the overall messenger mass scale $M_{\rm mess}$, a visible sector soft SUSY breaking mass scale, $\Lambda$ and $\tan\beta$. It also contains an additional discrete parameter, namely $N_{\rm mess}$, the number of SU(5) $5 \oplus \bar{5}$ representations of mediating fields. The example of a moduli mediated model which we consider is the large volume scenario derived in the context of $IIB$ flux compactification [22–25] whose two extra-Standard Model parameters can be parametrized by a universal scalar mass $m_0$ and $\tan\beta$. At an intermediate scale of $10^{11}$ GeV, the LVS has a universal gaugino mass $M_{1/2} = \sqrt{3} m_0$ and a universal trilinear scalar coupling $A_0 = -\sqrt{3} m_0$.

In Sec. III following, we detail the predictions of the golden cascade edges, as well as the expected precision that would come from LHC measurements. We also specify the SU3 CMSSM benchmark. In Sec. IV, we summarize the statistics we shall use to perform hypothesis testing on the different SUSY breaking models, defining parameter ranges for the fits. The results of the hypothesis tests are given in Sec. V. We show that mGMSB cannot be discriminated from SU3 by the edge data alone. It is then examined in more detail. We sum up and conclude in Sec. VI.

## III. KINEMATIC EDGES AT SU3

The ATLAS Collaboration has published a series of studies on reconstructing SUSY benchmark points in the supersymmetry section of Ref. [26]. We are specifically interested in the study of the CMSSM SU3 benchmark point and associated mass reconstruction using kinematic endpoints from golden cascades. The input parameters for the SU3 point are shown in Table I. SU3 is a point in the bulk region of the parameter space with $m_{\chi_1^0} = 118$ GeV and $m_{\tilde{g}} = 720$ GeV. Its spectrum contains the mass ordering $m_{\chi_1^0} < m_{\tilde{l}} < m_{\chi_2^0} < m_{\tilde{q}}$ or $m_{\chi_1^0} < m_{\chi_2^0} < m_{\tilde{l}} < m_{\tilde{q}}$ so that the golden decay chain is active (in the latter case, the $\chi_2^0$ decay is three body as the $\tilde{l}$ is off shell). We note that the SU3 point has recently been ruled out by the ATLAS experiment's jets plus zero lepton missing transverse momentum search [1,27]. This does not matter for the purposes of the present paper: one must simply bear in mind that a heavier point will have decreased statistics, and consequently will require more luminosity to discriminate against other models.

TABLE I. Input parameters of the CMSSM SU3 benchmark point.

| Parameter | $m_0$ | $m_{1/2}$ | $A_0$ | $\tan\beta$ | sgn $\mu$ |
|---|---|---|---|---|---|
| Value | 100 GeV | 300 GeV | −300 GeV | 6 | +1 |

In the golden decay chain in Fig. 1, one may construct several Lorentz invariant quantities from the four momenta of the visible particles: the quark and leptons. These are predicted to have various maxima and minima, each predicted by the theory to be related to the masses of the supersymmetric particles involved in the cascade decay. We shall now detail this dependence, which differs depending on whether the $\chi_2^0$ decays through a two-body decay with an on-shell slepton ($m_{\chi_2^0} > m_{\tilde{l}}$) or a three-body decay ($m_{\chi_2^0} < m_{\tilde{l}}$). We now detail each case in turn, collecting the edge predictions from Refs. [5,28] for completeness.

### A. Prediction of kinematic edges with an on-shell slepton

One kinematic maximum that we use is the dilepton mass edge. In terms of the sparticle masses, it is predicted to be

$$m_{ll}^{\rm edge2} = \frac{(m_{\chi_2^0}^2 - m_{\tilde{l}}^2)(m_{\tilde{l}}^2 - m_{\chi_1^0}^2)}{m_{\tilde{l}}^2}. \tag{2.1}$$

There are two $lq$ edges, in ascending order $m_{lq({\rm low})}$ and $m_{lq({\rm high})}$, respectively. They are defined to be the maximum or minimum of various quantities for $m_{\chi_2^0} > m_{\tilde{l}}$:

$$m_{lq({\rm high})} = \max[m_{lq}^{nr}, m_{lq}^{far}], \tag{2.2}$$

$$m_{lq({\rm low})} = \min[m_{lq}^{nr}({\rm max}), m_{lq}^{far}({\rm max}), m_{lq}^{l}({\rm max})], \tag{2.3}$$

where the quantities on the right-hand side are defined to be

$$m_{lq}^{nr2}({\rm max}) = \frac{(m_{\tilde{q}}^2 - m_{\chi_2^0}^2)(m_{\chi_2^0}^2 - m_{\tilde{l}}^2)}{m_{\chi_2^0}^2}, \tag{2.4}$$

$$m_{lq}^{far2}(\max) = \frac{(m_{\tilde{q}}^2 - m_{\chi_2^0}^2)(m_{\tilde{l}}^2 - m_{\chi_1^0}^2)}{m_{\tilde{l}}^2}, \tag{2.5}$$

$$m_{lq}^{l2}(\max) = \frac{(m_{\tilde{q}}^2 - m_{\chi_2^0}^2)(m_{\tilde{l}}^2 - m_{\chi_1^0}^2)}{2m_{\tilde{l}}^2 - m_{\chi_1^0}^2}. \tag{2.6}$$

The $llq$ edge is defined as

$$m_{llq}^{\text{edge2}} = \max\left[\frac{(m_{\tilde{q}}^2 - m_{\chi_2^0}^2)(m_{\chi_2^0}^2 - m_{\chi_1^0}^2)}{m_{\chi_2^0}^2}, \frac{(m_{\tilde{q}}^2 - m_{\tilde{l}}^2)(m_{\tilde{l}}^2 - m_{\chi_1^0}^2)}{m_{\tilde{l}}^2}, \frac{(m_{\tilde{q}}^2 m_{\tilde{l}}^2 - m_{\chi_2^0}^2 m_{\chi_1^0}^2)(m_{\chi_2^0}^2 - m_{\tilde{l}}^2)}{m_{\chi_2^0}^2 m_{\tilde{l}}^2}\right] \tag{2.7}$$

unless $m_{\tilde{l}}^4 < m_{\tilde{q}}^2 m_{\chi_1^0}^2 < m_{\chi_2^0}^4$ and $m_{\chi_2^0}^4 m_{\chi_1^0}^2 < m_{\tilde{q}}^2 m_{\tilde{l}}^4$, in which case the right-hand side is equal to $(m_{\tilde{q}} - m_{\chi_1^0})^2$. For the $llq$ *threshold* variable, the prediction is

$$\begin{aligned} m_{llq}^{\text{thr2}} = \frac{1}{4m_{\tilde{l}}^2 m_{\chi_2^0}^2}[&2m_{\tilde{l}}^2(m_{\tilde{q}}^2 - m_{\chi_2^0}^2)(m_{\chi_2^0}^2 - m_{\chi_1^0}^2) + (m_{\tilde{q}}^2 + m_{\chi_2^0}^2)(m_{\chi_2^0}^2 - m_{\tilde{l}}^2)(m_{\tilde{l}}^2 - m_{\chi_1^0}^2) \\ &- (m_{\tilde{q}}^2 - m_{\chi_2^0}^2)\sqrt{(m_{\chi_2^0}^2 + m_{\tilde{l}}^2)^2(m_{\tilde{l}}^2 + m_{\chi_1^0}^2)^2 - 16m_{\chi_2^0}^2 m_{\tilde{l}}^4 m_{\chi_1^0}^2}]. \end{aligned} \tag{2.8}$$

This edge is the $m_{llq}$ minimum for all events for which $\frac{1}{\sqrt{2}} \leq m_{ll}/m_{ll}(\max) \leq 1$.

### B. Prediction of kinematic edges with three-body $\chi_2^0$ decay

When $m_{\chi_2^0} < m_{\tilde{l}}$, the $\chi_2^0$ decays via a virtual $\tilde{l}$ into leptons and $\chi_1^0$, and in this case the above Eqs. (2.1), (2.2), (2.3), (2.4), (2.5), (2.6), (2.7), and (2.8) should be altered to the following:

$$m_{ll}^{\text{edge2}} = (m_{\chi_2^0} - m_{\chi_1^0})^2, \tag{2.9}$$

$$m_{lq(\text{high})}^2 = \frac{(m_{\tilde{q}}^2 - m_{\chi_2^0}^2)(m_{\chi_2^0}^2 - m_{\chi_1^0}^2)}{2m_{\chi_2^0}^2}, \tag{2.10}$$

$$m_{lq(\text{low})} = \frac{m_{lq(\text{high})}}{\sqrt{2}}, \tag{2.11}$$

$$m_{llq}^{\text{edge2}} = \begin{cases} (m_{\tilde{q}}^2 - m_{\chi_1^0}^2)^2 & \text{if } m_{\chi_2^0}^2 > m_{\tilde{q}} m_{\chi_1^0}, \\ (m_{\tilde{q}}^2 - m_{\chi_2^0}^2)(m_{\chi_2^0}^2 - m_{\chi_1^0}^2)/m_{\chi_2^0}^2 & \text{otherwise}, \end{cases} \tag{2.12}$$

$$m_{llq}^{\text{thr2}} = \frac{(m_{\chi_2^0} - m_{\chi_1^0})^2}{2} + \frac{m_{\tilde{q}}^2 - m_{\chi_2^0}^2}{4m_{\chi_2^0}^2}(3m_{\chi_2^0}^2 - m_{\chi_1^0}^2 - 2m_{\chi_2^0} m_{\chi_1^0} - \sqrt{m_{\chi_2^0}^4 + m_{\chi_1^0}^4 + 4m_{\chi_2^0} m_{\chi_1^0}(m_{\chi_2^0}^2 + m_{\chi_1^0}^2) - 10m_{\chi_2^0}^2 m_{\chi_1^0}^2}). \tag{2.13}$$

There is obviously less information than in the case where the slepton is on shell, because there are less constraints coming from four-momentum conservation. In particular, we see that $m_{\tilde{l}}$ does not feature in the equations, and there is no information on its mass held in the kinematic edges.

### C. ATLAS reconstruction of the edges

ATLAS have calculated the expected positions of the $m_{ll}^{\text{edge}}$, $m_{llq}^{\text{edge}}$, $m_{llq}^{\text{thr}}$, $m_{lq(\text{low})}$ and $m_{lq(\text{high})}$ mass distributions. We recalculate these using the spectrum obtained for the SU3 point from SOFTSUSY3.1.7 [29]. We take into account the possibility that $m_{\tilde{l}} > m_{\chi_2^0}$ leading to a three-body decay [28].[1] Since it is not possible to reconstruct the individual squark masses or flavor, we consider $m_{\tilde{q}_L}$ to be the average of the masses of the $\tilde{u}_L$ and $\tilde{d}_L$ squarks, as do ATLAS. In

[1]The presence of the two-body versus the three-body decay can affect the shape of the distribution of the dilepton invariant mass. We do not take this into account into our fits, considering only the position of the edge and not its shape.

TABLE II. This table shows the position of the endpoints and thresholds for the SU3 CMSSM point in GeV. The column labeled "ATLAS theory" is as predicted by ISAJET7.75 [30] and used in the experiment's simulations. The simulations of SUSY signal events in 1 fb$^{-1}$ of 14 TeV LHC collisions yielded the values marked in the reconstruction column. The final column shows the SU3 values predicted by SOFTSUSY3.1.7.

| Mass distribution | ATLAS theory | Reconstruction | SOFTSUSY3.1.7 |
|---|---|---|---|
| $m_{ll}^{\text{edge}}$ | 100.2 | 99.7 ± 1.4 | 103.9 |
| $m_{llq}^{\text{edge}}$ | 501 | 517 ± 33.7 | 532 |
| $m_{llq}^{\text{thr}}$ | 249 | 265 ± 23.7 | 265 |
| $m_{lq(\text{low})}$ | 325 | 333 ± 11.7 | 344 |
| $m_{lq(\text{high})}$ | 418 | 445 ± 19.0 | 446 |

Table II we show the positions of the edges as calculated by ATLAS, and those which we obtain from SOFTSUSY3.1.7. For the dilepton edges, the SOFTSUSY3.1.7 values are approximately 4 GeV higher than those given by ATLAS, and for the edges and thresholds involving quarks the discrepancy is larger, around 20–30 GeV. We have also checked that all the models possess the necessary mass ordering for all edges to exist simultaneously in at least some part of their parameter space. For instance, in mAMSB this can be achieved when $m_{\text{aux}}/m_0 \sim 10$. At the test point, $\tilde{q}_L$ and $\tilde{l}_R$ are the squarks and sleptons involved in the chain, and so we use $m_{\tilde{l}} = m_{\tilde{l}_R}$ and $m_{\tilde{q}} = m_{\tilde{q}_L}$ in Eqs. (2.1), (2.2), (2.3), (2.4), (2.5), (2.6), (2.7), (2.8), (2.9), (2.10), (2.11), (2.12), and (2.13). In general, one is unlikely to be able to deduce the sublabels $L$ or $R$ in the decay chain from the measurements alone. We check that allowing the labels to vary does not change the hypothesis testing results in Sec. V D.

With the SU3 spectrum, ATLAS simulated 1 fb$^{-1}$ of LHC data at $\sqrt{s} = 14$ TeV center-of-mass energy and simulated the reconstruction of the positions of the edges and thresholds. Full details are available in Ref. [26]. The results of this reconstruction are shown in column three of Table II, which shows the central values of the reconstructed edges and an estimate of the total error which is arrived at by combining in quadrature the estimated statistical, systematic and jet energy scale errors. For each edge, we further assume a theoretical error on the SOFTSUSY3.1.7 prediction of the edge of half of the difference between the SOFTSUSY3.1.7 prediction and the number under the ATLAS theory column of the table. We fit the four SUSY breaking models listed in Sec. II to the reconstructed endpoints in Table II. We have thus neglected the correlations in jet energy scale and other systematic errors. This should be a reasonable approximation for our purposes, and is conservative in the sense that including the correlations would actually *decrease* the total error volume. Thus, if we conclude that two models may be discriminated by including the errors independently, we may conclude that they would also be discriminated by including the measurement correlations.

## IV. INFERENCE AND FIT DETAILS

Assuming some model hypothesis $H$, Bayesian statistics help update a probability density function (PDF) $p(\underline{m}|H)$ of model parameters $\underline{m}$ with data. The prior encodes our knowledge or prejudices about the parameters. Since $p(\underline{m}|H)$ is a PDF in $\underline{m}$, $\int p(\underline{m}|H)d\underline{m} = 1$, which defines a normalization of the prior. One talks of priors being "flat" in some parameters, but care must be taken to refer to the measure of such parameters. A prior that is flat between some ranges in a parameter $m_1$ will not be flat in a parameter $x \equiv \log m_1$, for example. The impact of the data is encoded in the likelihood, or the PDF of obtaining data set $\underline{d}$ from model point $\underline{m}$: $p(\underline{d}|\underline{m}, H) \equiv \mathcal{L}(\underline{m})$. The likelihood is a function of $\chi^2$, i.e., a statistical measure of how well the data are fit by the model point. One useful quantity is the posterior; the PDF of the model parameters $m$ given some observed data $\underline{d}$ and assuming hypothesis $H$: $p(\underline{m}|\underline{d}, H)$. Bayes' theorem states that

$$p(\underline{m}|\underline{d}, H) = \frac{p(\underline{d}|\underline{m}, H)p(\underline{m}|H)}{p(\underline{d}|H)}, \tag{3.1}$$

where $p(\underline{d}|H) \equiv \mathcal{Z}$ is the Bayesian evidence, the probability density of observing data set $d$ integrated over all model parameter space. The Bayesian evidence is given by

$$\mathcal{Z} = \int \mathcal{L}(\underline{m})p(\underline{m}|H)d\underline{m}, \tag{3.2}$$

where the integral is over $N$ dimensions of the parameter space $\underline{m}$. We note that the evidence depends upon the ranges of $\underline{m}$ assumed.

In order to select between two models $H_0$ and $H_1$, one needs to compare their respective posterior probabilities given the observed data set $\underline{d}$, as follows:

$$\frac{p(H_1|\underline{d})}{p(H_0|\underline{d})} = \frac{p(\underline{d}|H_1)p(H_1)}{p(\underline{d}|H_0)p(H_0)} = \frac{\mathcal{Z}_1}{\mathcal{Z}_0}\frac{p(H_1)}{p(H_0)}, \tag{3.3}$$

where $p(H_1)/p(H_0)$ is the prior probability ratio for the two models, which we set to unity as we adopt the position that no mechanism of mediation is *a priori* more likely than any other. It can be seen from Eq. (3.3) that Bayesian model selection revolves around the evaluation of the Bayesian evidence. As the average of likelihood over the prior, the evidence automatically implements Occam's razor. A theory with fewer parameters has a higher prior density since it integrates to 1 over the whole space. Indeed, a theory with the same number of parameters but larger *a priori* parameter ranges will have a correspondingly smaller evidence, for a similar reason, provided both ranges cover the high likelihood region. There is thus a preference for fewer parameters and smaller ranges, unless the data strongly require there be more. Evaluation of the evidence is a computationally intensive task, and specific algorithms are required to make it practically possible. We use the nested sampling approach of Ref. [31] to evaluate the evidence. A by-product of this approach is that it also

produces posterior inferences. This method is implemented by the MULTINEST algorithm of Refs. [32,33] which we use in this paper.

The natural logarithm of the ratio of posterior model probabilities quantifies the level of discrimination between two models:

$$\Delta \log \mathcal{Z} = \log\left[\frac{p(H_1|\underline{d})}{p(H_0|\underline{d})}\right] = \log\left[\frac{\mathcal{Z}_1}{\mathcal{Z}_0}\frac{p(H_1)}{p(H_0)}\right]. \quad (3.4)$$

We summarize the convention we use in this paper in Table III.

In Bayesian model selection the results will always depend to some extent on the priors. Rather than seeking a unique ''right'' prior, one should check the independence of conclusions with respect to a reasonable variation of the priors. Such a sensitivity analysis is required to ensure that the resulting model comparison is not overly dependent on a particular choice of prior and the associated metric in parameter space, which controls the value of the integral involved in the computation of the Bayesian evidence. Prior dependence has been studied in the CMSSM fitted to indirect data in Ref. [34], where it was demonstrated that the indirect data were not constraining enough to allow a prior-independent determination of the preferred regions of the parameter space. Prior dependence in parameter estimation was also treated in Refs. [35,36], and in evidence evaluation in Refs. [18,37].

We have considered two different prior PDFs in this analysis. The first is the standard ''linear prior'' where $p(m_1) = p(m_2)$ for $m_{1,2}$ being two different points in the parameter space of one of the models under consideration. We shall contrast the results with linear priors versus those with log priors: each parameter $m$ with dimensions of mass has a prior whose distribution is flat in $\log(m)$, except for $A_0$ in the CMSSM. $A_0 = 0$ requires a different treatment because of the singularity at 0 in $\log A_0$: we choose a prior that is flat in $\log(|A_0| + C)$. For this particular study, we pick $C = 60$ GeV, but the results are not at all sensitive to the value chosen (indeed, we shall see that they are not sensitive to the choice of log or flat priors—a much larger change).

Before proceeding, we specify the parameter ranges over which we sample for the different models. We consider only the positive sign of $\mu$, as it is well known that the kinematical edges we consider do not have the power to distinguish the sign of $\mu$. It is unlikely that the LHC will have enough data to distinguish different signs of $\mu$: given current search constraints where soft SUSY breaking terms are expected to be heavy, the sign of $\mu$ may only have a fairly small effect on aspects of the spectrum. It affects heavier chargino and neutralino masses and mixings, and the third family sfermion mixings, all of which will be difficult to measure accurately at the LHC (but which may well be accurately measured at a future linear collider). The ranges over which we vary the continuous model parameters are shown in Table IV.

We bound $\tan\beta$ from below by 2, as values lower than this are in contravention of LEP2 Higgs searches, and from above by 62, since such large values lead to nonperturbative Yukawa couplings below the GUT scale and calculability is lost. In mGMSB the discrete parameter $N_{\rm mess}$, the number of messenger multiplets, is varied between 1 and 8. Higher values of $N_{\rm mess}$ lead to problems with perturbativity of gauge interactions at the GUT scale [21]. We wish to avoid possible contributions from gravity mediation in our mGMSB fits. Gravity mediated contributions will always be present and of order $F/M_{Pl}$, where $\sqrt{F}$ is the supersymmetry breaking scale, and we require these contributions to the soft masses to be less than 1 GeV. This implies a maximum value of $F$ of around $10^{19}$ GeV. Since the mass scale $\Lambda = F/M_{\rm mess} \sim 10^5$ GeV, we restrict $M_{\rm mess}$ to be less than $10^{14}$ GeV. In the CMSSM the unification scale is the standard GUT scale $M_{\rm GUT} \approx 2 \times 10^{16}$ GeV, while for the LVS the soft terms are defined at the intermediate string scale $m_s \approx 10^{11}$ GeV as in Ref. [25].

The constraints we use are all shown in Table II. We treat the measurements $D_i$ of the observables as independent. We also assume Gaussian errors on all measurements. The pull of observable $i$ is calculated by

$$s_i = \frac{|c_i - p_i|}{\sigma_i}, \quad (3.5)$$

where $c_i$ is the central experimental value of observable $i$, $p_i$ is the prediction of it by the model point and hypothesis assumed and $\sigma_i$ is the standard deviation incorporating both experimental and theoretical uncertainties, added in quadrature. The pull is a measure of how far the prediction is from the central experimental value in comparison to the

TABLE III. The Jeffreys' scale of hypothesis testing. Here the ''log'' represents the natural logarithm.

| $\lvert\Delta \log \mathcal{Z}\rvert$ | Odds | Probability | Remark |
|---|---|---|---|
| $<1.0$ | $\lesssim 3{:}1$ | $<0.750$ | Inconclusive |
| 1.0 | $\sim 3{:}1$ | 0.750 | Weak Evidence |
| 2.5 | $\sim 12{:}1$ | 0.923 | Moderate Evidence |
| 5.0 | $\sim 150{:}1$ | 0.993 | Strong Evidence |

TABLE IV. Ranges for the parameters in mGMSB and the large volume scenario. In mGMSB we also vary the discrete parameter $N_{\rm mess}$ between 1 and 8. For all models, $2 \leq \tan\beta \leq 62$.

| CMSSM | mAMSB |
|---|---|
| 1 GeV $\leq m_0 \leq$ 2 TeV | 1 GeV $\leq m_0 \leq$ 2 TeV |
| 60 GeV $\leq m_{1/2} \leq$ 2 TeV | 20 TeV $\leq m_{\rm aux} \leq$ 100 TeV |
| $-4$ TeV $\leq A_0 \leq$ 4 TeV | |
| mGMSB | LVS |
| $10^4$ GeV $\leq \Lambda \leq 10^6$ GeV | 1 GeV $\leq m_0 \leq$ 2 TeV |
| $10^5$ GeV $\leq M_{\rm mess} \leq 10^{14}$ GeV | |

error. In the limit of large statistics, where the experimental measurements have Gaussian probability distributions, $\chi^2 = \sum_i s_i^2$ follows a well-known ("$\chi^2$") distribution. The log likelihood of a prediction $p_i$ of an observable $i$ is given by

$$\log \mathcal{L}_i = -\frac{s_i^2}{2} - \frac{1}{2}\log(2\pi) - \log(\sigma_i). \tag{3.6}$$

The combined log likelihood is the sum of the individual log likelihoods,

$$\log \mathcal{L}^{\text{tot}} = \sum_i \log \mathcal{L}_i. \tag{3.7}$$

We do not use any indirect observables in this paper. If an edge or threshold is not present due to the mass ordering in the spectrum, the likelihood of that point is set to zero. Equation (3.7) amounts to assuming that the measurements of each endpoint are independent. This is not strictly true: jet-energy scale errors, for instance, will tend to correlate $m_{llq}^{\text{edge}}$, $m_{llq}^{\text{thr}}$, $m_{lq(\text{low})}$ and $m_{lq(\text{high})}$. However, this is not expected to be a large effect, and neglecting the resulting correlation should yield a reasonable approximation. Correlations between the sparticle masses coming from the measurements are automatically taken into account by Eqs. (2.1), (2.2), (2.3), (2.4), (2.5), (2.6), (2.7), and (2.8).

Aside from the Bayesian evidence, we shall evaluate the comparative quality of fit of each model via the $p$ value of their best-fit points. For a given model, the best-fit point in parameter space is defined to be the one with the lowest $\chi^2$. The $p$ value is constructed as follows: it is the probability of obtaining $\chi^2$ at least as large as the one actually observed $\chi_o^2$, assuming the best-fit point of the hypothesized model

$$p = \int_{\chi_o^2}^{\infty} \frac{1}{2^{k/2}\Gamma(k/2)} x^{k/2-1} e^{-x/2} dx, \tag{3.8}$$

where $k$ is the number of degrees of freedom: the number of observables minus the number of parameters in the model. $p$ values do not depend upon priors. However, in common problems, the interpretation of the $p$ value is problematic because of the identification of the number of degrees of freedom. One could always add additional observables that are insensitive to the value of the model parameters at the best-fit point, changing the value of $p$, for instance. Also, the presence of physical boundaries may spoil the interpretation of $p$ as calculated in Eq. (3.8) [38]. Nevertheless, we use $p$ values as a qualitative estimator of the overall quality of the fit in each case: a small $p$ value indicates the fact that the model is not able to fit the data well, and a $p$ value closer to unity indicates that the model may fit it. We calculate the $p$ value by minimizing the $\chi^2$ function using the minimizer MINUIT [39] (a particular configuration of MULTINEST has also shown to be able to perform this task [40]). We use the point sampled by MULTINEST during the evidence calculation with the highest likelihood as a starting seed.

Since we are assuming that the LHC measurements discover missing transverse momentum like signals, which yield SUSY signals leading to the endpoints detailed in Table II, we require a neutral MSSM particle that is stable, at least on time scales required for it to traverse a LHC detector. Therefore, in mAMSB, the CMSSM and the LVS the neutralino must be the lightest supersymmetric particle (LSP), or else we set the likelihood to zero. In mGMSB the gravitino $\tilde{G}$ is the LSP, and the collider signatures are to a large part determined by the identity of the next-to-lightest supersymmetric sparticle (NLSP). If the stau is the NLSP we reject the point, assigning it a zero likelihood. If the neutralino is the NLSP we consider its decay length. If the (binolike) neutralino decays inside the detector, then the classic diphoton and missing transverse energy of low scale mGMSB is realized, in contradiction to the signals that we assume from Ref. [26]. We therefore ensure that in mGMSB the NLSP is the neutralino and that it is stable on detector time scales. Specifically, we calculate the decay length of the neutralino according to Ref. [41] where

$$L_{\text{decay}} = \frac{1}{\kappa_\gamma}\left(\frac{100\ \text{GeV}}{m_{\text{NLSP}}}\right)^5 \left(\frac{\Lambda}{100\ \text{TeV}}\right)^2 \times \left(\frac{M_{\text{mess}}}{100\ \text{TeV}}\right)^2 10^{-4}\ \text{m}, \tag{3.9}$$

where $\kappa_\gamma$ is the photino component of the neutralino, since in mGMSB the neutralino NLSP is predominantly photino-like. If the decay length is less than 10 m we reject the point. We also apply some simple direct search bounds, adapted from Refs. [18,42,43]. If a sparticle mass fails to satisfy these bounds, the corresponding point is assigned a zero likelihood.

To calculate the MSSM spectrum we use SOFTSUSY3.1.7 which calculates the spectrum of the CMSSM, mAMSB and mGMSB. By modifying the unification scale from $M_{\text{GUT}}$ to $m_{\text{string}} \sim 10^{11}$ GeV and by not enforcing gauge coupling unification, SOFTSUSY3.1.7 can also provide the spectrum in the LVS case. Parameter space points which do not break electroweak symmetry correctly or have tachyonic sparticles are assigned zero likelihood. However, this disallowed part of parameter space *is* included in our calculation of the prior volume and so will consequently reduce the evidence. Points which have a charged LSP are rejected.[2]

[2]Due to the small neutralino-chargino splitting in mAMSB we must reject any points that would violate the long-lived charged stable particle bounds from Tevatron, which requires $\Delta m = m_{\chi_1^+} - m_{\chi_1^0} > 50$ MeV. In practice, we find that this bound does not constrain the mAMSB parameter space since mAMSB predicts larger splittings [44].

TABLE V. Hypothesis testing statistics for the different models. The columns labeled $Z$ show the Bayesian evidence for either linear or logarithmic priors. The error on each entry of the Bayesian $\log Z$ delivered by MULTINEST is $\pm 0.1$.

| Model | $\log Z$ (linear) | $\log Z$ (logarithmic) | $p$ value |
|---|---|---|---|
| CMSSM | $-28.1$ | $-25.1$ | 0.64 |
| mGMSB | $-27.1$ | $-25.8$ | 0.83 |
| mAMSB | $-55.7$ | $-54.1$ | $<10^{-10}$ |
| LVS | $-47.0$ | $-47.0$ | $1.4 \times 10^{-9}$ |

## V. FITS TO EDGE DATA

### A. Hypothesis testing

The Bayesian evidence values calculated for the different models and priors are shown in Table V. Although there is a small dependence of the evidence upon the prior, there is a much larger difference between the evidences of some of the models and so we may expect to reliably discriminate between them on that basis. One would strongly discriminate against the LVS and mAMSB in favor of SU3 based either on the Jeffreys' scale of Bayesian evidence differences or on the $p$ values. However, we see that we would not discriminate between mGMSB and the CMSSM using the evidence. Reassuringly, the $p$ values point in the same direction as the Bayesian evidence: mAMSB and the LVS would be discriminated against, but mGMSB and the CMSSM could not be distinguished on the basis of edge data alone. The agreement of the interpretation of the naive frequentist ($p$ value) and Bayesian (evidence) measures of hypothesis test is another signal that the fits are fairly robust, together with their approximate prior independence.

### B. Best-fit points

The best-fit points along with their $\chi^2$ values divided by the number of degrees of freedom ($\chi^2$/d.o.f.) and the associated $p$ value are shown in Table VI. The table illustrates that SOFTSUSY3.1.7 is able to fit the $\mu > 0$ CMSSM to the assumed edge variables extremely well, despite the fact that they were produced by a different SUSY spectrum calculator. This is implied by the statement that there are only small differences in the masses of sparticles appearing in the golden decay chain between the spectrum calculators anyway, as Ref. [13] shows. Performing another fit for $\mu < 0$, we confirm our earlier assertion that the edges we study are not sensitive to the sign of $\mu$, obtaining a total $\chi^2$ of 0.14 and a $p$ value of 0.71. Similar fits are obtained for the other models under study for $\mu < 0$ as for $\mu > 0$, and so we simply show results of the fits for $\mu > 0$. Non-LHC data may separate the two signs of $\mu$: famously, the anomalous magnetic moment of the muon is sensitive to it (and prefers $\mu > 0$ in the CMSSM). Also, linear collider measurements of neutralinos and charginos may accurately constrain all of the parameters appearing in their mixing matrices, including $\mu$ [45]. While we display only the absolute best-fit point in the table for mGMSB, there are in fact best-fit points for $N_5 = 3$, 4 and 6 which have $p$ values larger than 0.05, indicating that one would not necessarily discriminate against mGMSB with these values of $N_5$ either.

We plot the spectra of the CMSSM and mGMSB best-fit points in Fig. 2. The decays were calculated with HERWIG++-2.5.2 [46–48], and we display only those decays whose branching ratios are higher than 10%. The figure shows that the two best-fit spectra and decays are remarkably similar, and could prove difficult to discriminate. Although the heavier third generation squarks are somewhat heavier in mGMSB, they may be difficult to access experimentally because decays to them from the gluino are phase-space suppressed. Although, in the mGMSB panel, the decay of $\chi_1^0$ to gravitino (ejecting a photon) is shown, the neutralinos are actually quasistable and so this decay will not show up in the experiment. We find that the decay length of the neutralino for the best-fit point is about 12.5 AU, due to the very high messenger scale. The splitting between gluino and first two generations of squark (denoted $\tilde{q}_L$ and $\tilde{q}_R$, respectively, in the figure) are smaller for mGMSB, which could potentially make one of the jets from gluino decay softer, so there could be a potential discriminator in the hardness of this jet, or indeed the multiplicity from gluino decays, if the jet is too soft to make it past jet cuts. A feasibility study of experimental separation between these two models would require a detailed study, and is beyond the scope of this paper. Figure 3

TABLE VI. Best-fit points (defined as having the highest likelihood) for each model, along with the associated value of $\chi^2$/d.o.f. and $p$ value. We have assumed that $\mu > 0$ for each point.

| Model | Parameters | $\chi^2$/d.o.f. | $p$ value |
|---|---|---|---|
| CMSSM | $m_0 = 92.1$ GeV, $m_{1/2} = 300.6$ GeV<br>$A_0 = 984$ GeV, $\tan\beta = 12.3$ | 0.22/1 | 0.64 |
| mAMSB | $m_{\rm aux} = 28.46$ TeV, $m_0 = 255.5$ GeV<br>$\tan\beta = 22.4$ | 52/2 | $<10^{-10}$ |
| mGMSB | $M_{\rm mess} = 1.010^{14}$ GeV, $\Lambda = 1.7810^4$ GeV<br>$N_5 = 5$, $\tan\beta = 22.2$ | 0.36/2 | 0.83 |
| LVS | $m_0 = 359$ GeV, $\tan\beta = 4.75$ | 44.2/3 | $1.4 \times 10^{-9}$ |

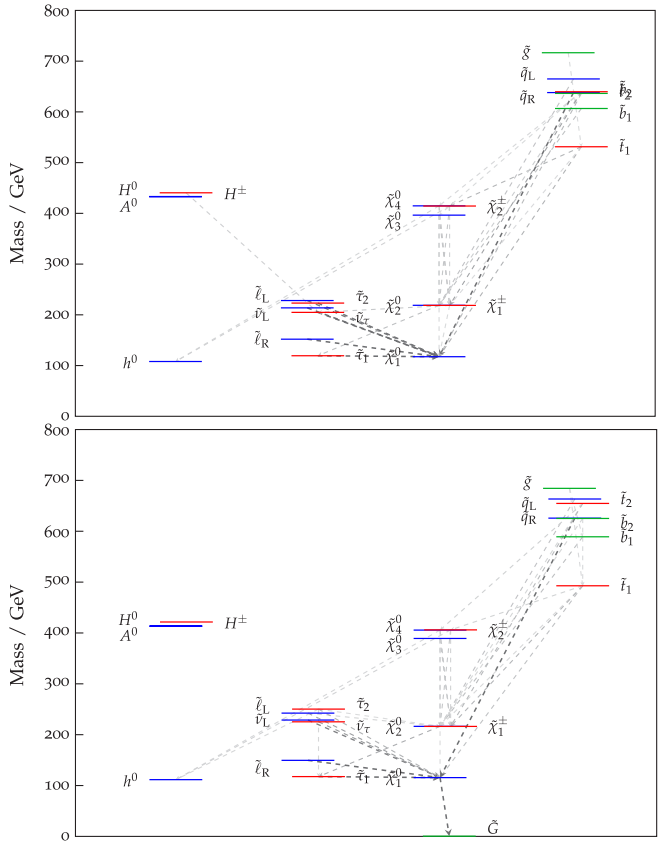


FIG. 2 (color online). Spectra and decays in the best-fit points of the CMSSM (top panel) and mGMSB (bottom panel). Here, neutralinos and charginos are displayed with tildes, unlike in the rest of the paper.

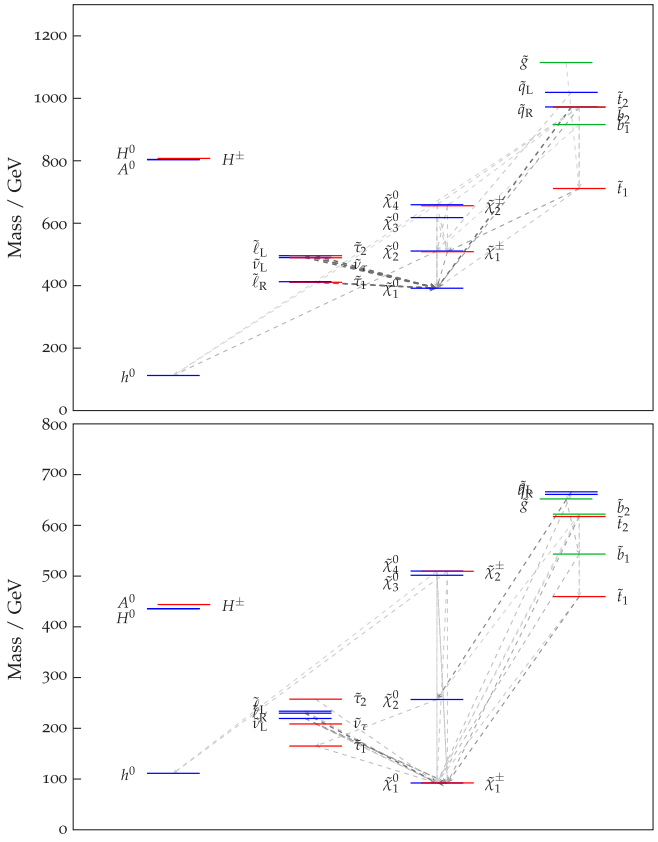


FIG. 3 (color online). Spectra and decays in the best-fit points of the LVS (top panel) and mAMSB (bottom panel). Here, the neutralinos and charginos are displayed with tildes, unlike in the rest of the paper.

displays the spectra and decays that have branching ratios higher than 10% for the best-fit the LVS and mAMSB points. A comparison of either model with the best-fit CMSSM spectrum displayed in Fig. 2 displays some obvious differences. In the LVS model, the two lightest neutralinos have a different splitting to the CMSSM model, and the $\tilde{l}_R - \chi^0_2$ mass splitting is also different. Also, the squarks are much heavier in the LVS model. In the best-fit mAMSB model, the $\tilde{l}_R$ is significantly heavier than in the best-fit CMSSM model.

What leads to the similarities between the mGMSB and CMSSM best-fit points' spectra? In the CMSSM the soft terms run from the GUT scale, while in mGMSB they run from the messenger scale $M_{\rm mess}$. We observe that the messenger scale of the mGMSB best-fit point is as close as possible to the GUT scale given the range assumed in Table IV, $M_{\rm mess} = 1 \times 10^{14}$ GeV. Working to one-loop order, since the ratio of each MSSM group's gaugino mass $M_i$ to its gauge coupling squared $g_i^2$ does not run, if there exists a renormalization scale $\mu = \mu_0$ for which

$$\frac{M_3(\mu)}{g_3(\mu)^2} = \frac{M_3(\mu)}{g_2(\mu)^2} = \frac{M_3(\mu)}{g_1(\mu)^2}, \tag{4.1}$$

then Eq. (4.1) applies for any $\mu$, in particular at the weak scale. In the CMSSM, Eq. (4.1) is satisfied because $M_3(M_{\rm GUT}) = M_2(M_{\rm GUT}) = M_1(M_{\rm GUT})$ as well as $g_3(M_{\rm GUT}) = g_2(M_{\rm GUT}) = g_1(M_{\rm GUT})$, whereas the mGMSB soft SUSY breaking boundary conditions are $M_i(M_{\rm mess}) = N_5 \Lambda g_i^2(M_{\rm mess}) f/(16\pi^2)$ [41], where $f$ is a dimensionless number depending upon parameter space (but not on the gauge group $i$). The mGMSB gaugino masses thus explicitly satisfy Eq. (4.1) in a different way to the CMSSM at $\mu = M_{\rm mess}$. Numerically, substituting $\mu = M_Z$ into Eq. (4.1) leads to the approximate pattern $M_3{:}M_2{:}M_1 \sim 6{:}2{:}1$ for the weak-scale gaugino masses, which applies to both mGMSB and the CMSSM.

The high-scale scalar mass boundary conditions in mGMSB have more complicated expressions than in the CMSSM, as they depend on the quadratic Casimir operators and $g_i$. They are not universal at the GUT scale. We find that the SUSY breaking right-handed slepton mass parameter for the best-fit mGMSB point at the GUT scale is 92.8 GeV, close to the CMSSM value of 92.4 GeV. The left-handed slepton mass parameters are somewhat larger as they are charged under $SU(2)$, but at the weak scale it is the right-handed sleptons which are lightest and whose

mass parameters we use to calculate the edge positions. This difference therefore does not affect the quality of the fit. The mGMSB squark masses at the messenger scale are significantly different to the CMSSM squark masses which are given by $m_0$. However, during the renormalization group running, the squark masses are renormalized by the contributions from the gluino, and thus at the low scale the squark masses for both model points are similar to the gluino mass. Finally, the trilinear $A$ terms differ for the CMSSM and mGMSB best-fit points, but they affect the endpoints by less than 1%. We display the renormalization of the most relevant mass parameters in Fig. 4. Since $\chi_1^0$ and $\chi_2^0$ are approximately bino- and wino-dominated, respectively, tuning $\Lambda$ allows mGMSB to match both gaugino masses to the ones required by our benchmark CMSSM point in the 2:1 ratio that applies to both models. The other messenger scale scalar masses are fixed, but we may then tune $M_{\rm mess}$ to get one of them [say, $m_{\tilde{e}_R}(M_{\rm mess})$] to match with its equivalent value in the CMSSM benchmark. The other mass [in this case $m_{\tilde{q}_R}(M_{\rm mess})$] is then predicted by mGMSB, and must renormalize (within an accuracy dictated by the measurement errors) to the tree-level value in the CMSSM benchmark model. We see from Fig. 4 that this is indeed the case.

The pulls from each observable $s_i$ are displayed in Fig. 5 for the best-fit mGMSB and CMSSM models. We see a similar pattern for each of the observables except for $m_{ll}^{\rm edge}$, which is larger for mGMSB. However, it is clear that each of the observables is well fit by each best-fit model, with no one observable dominating the $\chi^2$. Note that even though mGMSB has a higher value of $\chi^2$, it has a slightly higher $p$ value because it has less free continuous parameters, and therefore a larger number of degrees of freedom.

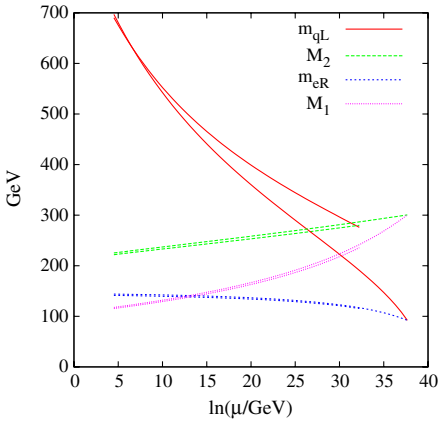


FIG. 4 (color online). Renormalization of CMSSM and mGMSB best-fit points. We show the most relevant $\overline{DR}$ mass parameters as a function of the renormalization scale $\mu$ for each model. The CMSSM model curves continue to $\ln(\mu/\text{GeV}) \approx 37$, whereas the mGMSB model curves terminate at $\ln(\mu/\text{GeV}) \approx 32$.

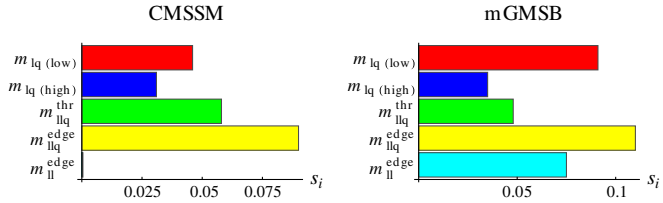


FIG. 5 (color online). Pulls in the best-fit points of the CMSSM and mGMSB.

We note that the edge information is not the only information one would collect about the models to use to discriminate them. Before sufficient statistics have been collected to constrain the kinematic edges, we would have rate data on the number of signal events passing cuts in missing transverse momentum type searches. The production rates of supersymmetric particles at the LHC typically dominantly depend upon the squark and gluino masses, since these are the strongly interacting particles with the largest direct production cross sections. They then decay in various ways into different channels. The rates for the individual channels do have a complicated dependence on the detailed MSSM parameters, but still all channels are proportional to the total SUSY production cross section, which is a function of squark and gluino masses only, to a good approximation. Therefore the total SUSY production cross section is a function of squark and gluino masses, and we compare them at the best-fit points of the CMSSM and mGMSB models in Table VII. We also show the total next-to-leading order SUSY production cross section as calculated by PROSPINO [49]. This is the cross section *without cuts or acceptance corrections*, so the measurable cross section will be some factor times smaller (around 30 in some examples). We see from Table VII that the CMSSM and mGMSB have similar squark and gluino masses, resulting in a similar total SUSY LHC production cross section. Thus, the models would likely require other

TABLE VII. Phenomenological properties of the best-fit points. We show some aspects of the mass spectra and the total next-to-leading order SUSY 14 TeV LHC production cross section $\sigma_{\rm NLO}$ of the best-fit points. $m_{\tilde{q}}$ is an averaged first family squark mass, $m_{h^0}$ is the lightest $CP$ even Higgs mass and $m_{A^0}$ is the $CP$ odd Higgs mass. The two branching ratios listed are the ones relevant for the golden decay chain.

| | CMSSM | mGMSB | LVS | mAMSB |
|---|---|---|---|---|
| $m_{\tilde{g}}$/GeV | 716 | 686 | 1116 | 652 |
| $m_{\tilde{q}}$/GeV | 662 | 662 | 1019 | 660 |
| $\sigma_{\rm NLO}$/pb | 22 | 25 | 1.7 | 29 |
| $m_{\tilde{\tau}_1} - m_{\chi_1^0}$/GeV | 2.0 | 2.4 | 19 | 73 |
| $m_{h^0}$/GeV | 108 | 111 | 112 | 111 |
| $m_{A^0}$/GeV | 430 | 411 | 803 | 436 |
| $BR(\tilde{q} \to qll\chi_1^0)$/% | 2.5 | 1.2 | 3.4 | 19.4 |
| $BR(\tilde{q} \to q\tau\tau\chi_1^0)$/% | 20.1 | 29.1 | 2.5 | 19.2 |

more detailed empirical information to tell them apart. If we scaled up the masses of all sparticles at the mGMSB and CMSSM points so that squarks and gluino masses are similar to the LVS best-fit point, we would have a total SUSY cross section of around 1/10th of the value that SU3 has. If the number of events which passed cuts just scaled with the total SUSY cross section, we would then expect to require 10 $\text{fb}^{-1}$ of LHC data in order to achieve similar fractional precisions on the endpoints as the ones assumed in the present paper. Of course, a dedicated simulation of LHC collisions would be required to calculate this number more exactly and to verify that for heavier spectra mGMSB is indeed able to emulate the CMSSM spectrum.

We also list some other properties of the best-fit points in Table VII to see if they might be discriminated on the basis of other observables. We also see that the Higgs masses are different between the CMSSM and mGMSB points. However, they are probably too similar for LHC measurements: the lightest CP even Higgs mass difference is just beyond the theoretical uncertainty in its prediction of $\pm 3$ GeV [13]. The 30 GeV difference in $m_{A^0}$ is unlikely to provide discrimination, since ATLAS studies indicate that even 300 $\text{fb}^{-1}$ are not expected to yield a $5\sigma$ discovery of the $A^0$ [50]. On the other hand, the total rate $\sigma_{\text{NLO}} \times BR(\tilde{q} \to qll\chi_1^0)$ (which may be known to the $\sim$10% level) for the dilepton channel in mGMSB is *half* that of the CMSSM, ought to discriminate well between the two models. $\sigma_{\text{NLO}} \times BR(\tilde{q} \to q\tau\tau\chi_1^0)$ may also be used to discriminate between the two models well.

### C. Posterior distributions for CMSSM and mGMSB

We now discuss some features of the posterior distributions for the models that are difficult to discriminate: the CMSSM and mGMSB. We do not present the frequentist bounds upon the parameters using $\Delta\chi^2$ because it has poor coverage properties [38]. Figure 6 shows the 2D posterior for log priors in the $m_0 - m_{1/2}$ plane for the correct

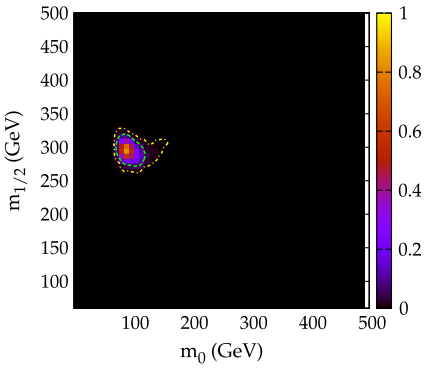


FIG. 6 (color online). Posterior PDF for the CMSSM in the $m_0 - m_{1/2}$ plane with log priors. The dashed green (inner) and dashed yellow (outer) contours show the 95% Bayesian confidence intervals for log and flat priors, respectively.

hypothesis for SUSY breaking, the CMSSM. It also shows the 95% Bayesian confidence interval contours for both sets of priors. The posterior is a localized single mode distribution, and the two contours lie on top of one another, demonstrating prior independence in this plane. This is not the case for the trilinear couplings $A_i$ which are not well constrained by the edges because these parameters have only a small effect on the mass spectrum to which our fits are sensitive. Our posteriors are in agreement with previous fits of the CMSSM using kinematic invariants [7,16,19].

Turning to mGMSB, Fig. 7 shows 1D posteriors for the mass scale $\Lambda$ and the logarithm of the messenger scale $\log_{10}(M_{\text{mess}})$ in GeV. We see from the left-hand panel that in contrast to the CMSSM, the posterior is strongly multimodal, irrespective of prior. This is because the physical masses in mGMSB are proportional to $N_{\text{mess}}\Lambda$, and $N_{\text{mess}}$ is a discrete parameter. Each peak in the posterior for $\Lambda$ corresponds to a different value for $N_{\text{mess}}$, with lower values of $\Lambda$ being associated with higher values of $N_{\text{mess}}$, since their product must be the mass scale given by the edge measurements. In the right-hand panel, we display the

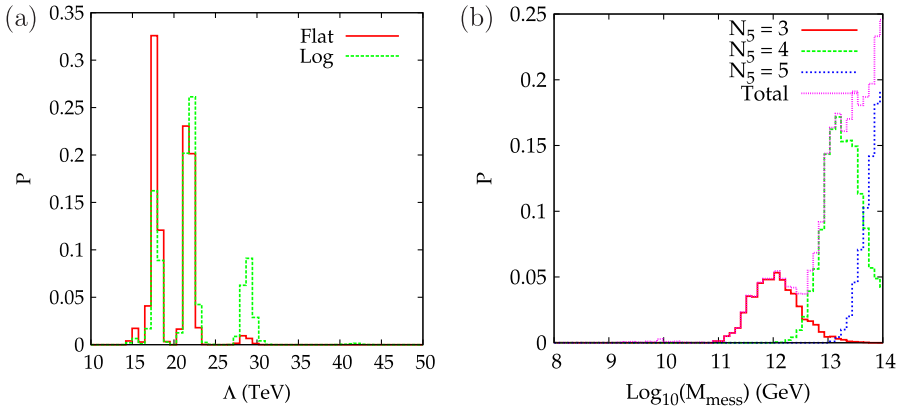


FIG. 7 (color online). Posterior PDFs for mGMSB. The left-hand panel shows the 1D posterior for the mass scale $\Lambda$ for both priors and the right-hand panel shows the 1D posterior for the messenger mass $M_{\text{mess}}$ assuming logarithmic priors. The right-hand panel also shows the decomposition of the posterior according to messenger number $N_{\text{mess}} = 3, 4, 5$.

TABLE VIII. Best-fit points for each model including the $m_{\tau\tau}^{\text{edge}}$ measurement, along with the associated value of $\chi^2$/d.o.f. and $p$ value. We have assumed that $\mu > 0$ for each point.

| Model | Parameters | $\chi^2$/d.o.f. | $p$ value |
|---|---|---|---|
| CMSSM | $m_0 = 93.3$ GeV, $m_{1/2} = 297.8$ GeV $A_0 = 5$ GeV, $\tan\beta = 7.8$ | 0.42/1 | 0.48 |
| mAMSB | $m_{\text{aux}} = 28.46$ TeV, $m_0 = 255.5$ GeV $\tan\beta = 22.4$ | 45.7/2 | $1.2 \times 10^{-10}$ |
| mGMSB | $M_{\text{mess}} = 1.010^{14}$ GeV, $\Lambda = 1.7910^{4}$ GeV $N_5 = 5$, $\tan\beta = 12.2$ | 0.71/2 | 0.30 |
| LVS | $m_0 = 362$ GeV, $\tan\beta = 4.77$ | 44.5/3 | $1.2 \times 10^{-9}$ |

posterior of $M_{\text{mess}}$ separated according to different values of $N_5$, as well as summed ("Total"). The $M_{\text{mess}}$ posterior extends down to $10^{11}$ GeV, having some substructure due to overlapping modes. There is a positive correlation between $M_{\text{mess}}$ and $N_{\text{mess}}$. From this we can infer that value of $N_{\text{mess}}$ larger than 5 would only be favored with unfeasibly high messenger scales. Low values of $M_{\text{mess}}$ require lower values of $N_{\text{mess}}$ in order to fit the data. Indeed, the MULTINEST algorithm identifies modes with $N_{\text{mess}} = 1, 2$, but these modes are of poor fit quality compared with those of intermediate messenger number $N_{\text{mess}} = 3$–$6$. This is a salutary lesson that fitting a low dimensional model to constraining data can still lead to a complicated mode structure in the posterior.

### D. Inclusion of $m_{\tau\tau}^{\text{edge}}$

Reference [26] also included the possible measurement of $m_{\tau\tau}^{\text{edge}}$, which is predicted by Eq. (2.1) with $\tilde{l} \to \tilde{\tau}$. This variable has a very different shape to $m_{ll}^{\text{edge}}$ since the $\tau$s decay to neutrinos, thus some of their energy is missing from any reconstruction. However, $m_{\tau\tau}$ still has a kinematic maximum (given by the events where the neutrinos' momenta vanish) and ATLAS fits it from a background subtracted event sample using a log normal distribution. Since the distribution is not at all sharp, the errors on the measurement of $m_{\tau\tau}^{\text{edge}}$ are much larger than that on $m_{ll}^{\text{edge}}$. ATLAS estimated that with 1 fb$^{-1}$ of 14 TeV data, they could measure

$$m_{\tau\tau}^{\text{edge}} = 102 \pm 20.2 \text{ GeV},$$

where we have added statistical and systematic errors in quadrature. We perform the $\chi^2$ fits again including this constraint in order to see whether it can help discriminate between mGMSB and the CMSSM, or whether it changes any aspect of the fits. We also take into account the fact that either $\tilde{q}_{L/R}$ or $\tilde{l}_{L/R}$ may take part in the golden decay chain, and would be indistinguishable for equal masses. We perform this check by calculating the branching ratios via the SUSY Les Houches Accord [51] and HERWIG++-2.5.2 [46–48]. The labels $L$ or $R$ are on the squark and slepton are chosen to be the ones yielding the largest branching ratios. These labels are then used for $m_{\tilde{l}}$ and $m_{\tilde{q}}$ in Eqs. (2.1), (2.2), (2.3), (2.4), (2.5), (2.6), (2.7), (2.8), (2.9), (2.10), (2.11), (2.12), and (2.13). The results are shown in Table VIII. Performing the fits again but assuming the labels are $\tilde{q}_L$ and $\tilde{l}_R$ yields identical results, within statistical uncertainties, validating our previous hypothesis tests.

We see from Table VIII that $m_{\tau\tau}^{\text{edge}}$ has not changed the conclusions from the previous fits at all: the CMSSM and mGMSB remain equally good fits, and the other two models considered are heavily disfavored. The best-fit points have not moved by much, except for $A_0$ which has a large uncertainty in the fit prediction: it is not very well constrained by the edge data. The inclusion of $m_{\tau\tau}^{\text{edge}}$ may make the uncertainties on inferred parameters slightly smaller in the posterior distributions of Sec. V C.

In principle, one could also attempt to constrain the models using $m_{\tau\tau q}$ and $m_{\tau q}$ endpoints, but ATLAS did not simulate measurements for these observables and so we do not use them here.

## VI. CONCLUSIONS

We have evaluated the ability of the LHC, through the measurement of kinematic end points in supersymmetric signals, to distinguish between different models of supersymmetry breaking with a small number of parameters. We find that the mAMSB and the LVS models can be unambiguously discriminated from our CMSSM benchmark model by the endpoints with just 1 fb$^{-1}$ of data. However, kinematic edges could not discriminate between the best-fit CMSSM and mGMSB models, the spectra of which turn out to be very similar (except for the gravitino mass, which is irrelevant for LHC signals because the lightest neutralino is quasistable). Reassuringly, one reaches these conclusions whether or not one uses Bayesian or frequentist statistics to perform the hypothesis test. This is additional confirmation that the sparticle spectrum is sufficiently constrained by the measurements in these models, and is confirmation of the fact that if a fit has sufficient data, a Bayesian interpretation will be approximately prior independent and give the same results as a frequentist interpretation. A previous study [19] found a significant prior dependence in models of SUSY breaking that have more parameters than the CMSSM. This is not so

surprising given that the number of parameters would outnumber the number of experimental constraints. In that case, we would not even be able to calculate the $p$ value, since the number of degrees of freedom would be negative, and the system is under constrained.

The best-fit mGMSB and CMSSM spectra look remarkably similar, but the *rate* for the golden decay chain differs by a factor of 2, and will provide the discrimination required between the two different models. It should also be possible to use a future direct detection of dark matter consistent with the CMSSM lightest neutralino mass in order to discriminate against mGMSB, whose gravitino LSP predicts zero direct detection cross section because it interacts too weakly.[3] One could also attempt to answer the question: what subspace of the CMSSM parameter space predicts observables that are close to those of mGMSB? We would not expect mGMSB to be able to mimic a focus-point spectrum with large $m_0$ but moderate $m_{1/2}$ for example, since this would result in a rather hierarchical mass pattern, which the relatively compressed spectra of mGMSB may find hard to reproduce. It is also true, however, that the focus point does not possess the golden decay chain and so different observables to the ones studied here would have to be examined.

[3]A recent study showed that forthcoming ton scale direct detection experiments will probe the majority of the CMSSM parameter space that currently fits indirect data well [52].

Kinematic endpoints of cascade decays are arguably the best tool for discriminating different SUSY breaking models from LHC data, since they are sensitive to the sparticle spectrum and do not require several hundred $\text{fb}^{-1}$ of integrated luminosity in order to parametrize the detector response well. In the case that cascades other than the golden one assumed here are present and identifiable, one would include their data. The fit is still likely to be dominated by the constraints coming from the golden cascade, however. The golden cascade utilized here may not be present, even in the event of a SUSY signal at the LHC. However, in that case other less constraining cascades will be used but are unlikely to provide the discriminating power that the golden one does. This study is therefore an estimate of the maximum discriminatory power one could have.

In summary, although kinematic endpoints deliver important information on the nature of SUSY breaking (discriminating against mAMSB, the LVS, and the CMSSM), there still may exist degeneracies between some models (for example, mGMSB and the CMSSM SU3 benchmark point). This degeneracy may be broken by using rate information of the golden cascade.

## ACKNOWLEDGMENTS

This work has been partially supported by STFC. We would also like to thank the IPPP for support under their associateship scheme. B. C. A. thanks other members of the Cambridge SUSY Working Group for helpful suggestions.

[1] G. Aad *et al.* (ATLAS Collaboration), Phys. Lett. B **701**, 186 (2011).
[2] V. Khachatryan *et al.* (CMS Collaboration), Phys. Lett. B **698**, 196 (2011).
[3] D. Miller, P. Osland, and A. Raklev, J. High Energy Phys. 03 (2006) 034.
[4] I. Hinchliffe, F. Paige, M. Shapiro, J. Soderqvist, and W. Yao, Phys. Rev. D **55**, 5520 (1997).
[5] B. C. Allanach, C. G. Lester, M. A. Parker, and B. R. Webber, J. High Energy Phys. 09 (2000) 004.
[6] B. K. Gjelsten, D. J. Miller, and P. Osland, J. High Energy Phys. 12 (2004) 003.
[7] C. G. Lester, M. A. Parker, and M. J. White, J. High Energy Phys. 01 (2006) 080.
[8] G. Weiglein *et al.* (LHC/LC Study Group Collaboration), Phys. Rep. **426**, 47 (2006).
[9] G. Blair, W. Porod, and P. Zerwas, Phys. Rev. D **63**, 017703 (2000).
[10] G. Blair, W. Porod, and P. Zerwas, Eur. Phys. J. C **27**, 263 (2003).
[11] B. Allanach, G. Blair, S. Kraml, H. Martyn, G. Polesello *et al.*, arXiv:hep-ph/0403133.
[12] B. Allanach, D. Grellscheid, and F. Quevedo, J. High Energy Phys. 05 (2002) 048.
[13] B. Allanach, S. Kraml, and W. Porod, J. High Energy Phys. 03 (2003) 016.
[14] P. Bechtle, K. Desch, M. Uhlenbrock, and P. Wienemann, Eur. Phys. J. C **66**, 215 (2010).
[15] R. Lafaye, T. Plehn, M. Rauch, and D. Zerwas, Eur. Phys. J. C **54**, 617 (2008).
[16] L. Roszkowski, R. R. de Austri, and R. Trotta, Phys. Rev. D **82**, 055003 (2010).
[17] H. K. Dreiner, M. Kramer, J. M. Lindert, and B. O'Leary, J. High Energy Phys. 04 (2010) 109.
[18] S. S. AbdusSalam, B. C. Allanach, M. J. Dolan, F. Feroz, and M. P. Hobson, Phys. Rev. D **80**, 035017 (2009).
[19] A. Fowlie and L. Roszkowski, arXiv:1106.5117.
[20] L. Randall and R. Sundrum, Nucl. Phys. **B557**, 79 (1999).
[21] G. F. Giudice and R. Rattazzi, Phys. Rep. **322**, 419 (1999).
[22] V. Balasubramanian, P. Berglund, J. P. Conlon, and F. Quevedo, J. High Energy Phys. 03 (2005) 007.
[23] J. P. Conlon, F. Quevedo, and K. Suruliz, J. High Energy Phys. 08 (2005) 007.

[24] J. P. Conlon, S. S. Abdussalam, F. Quevedo, and K. Suruliz, J. High Energy Phys. 01 (2007) 032.
[25] B. C. Allanach, M. J. Dolan, and A. M. Weber, J. High Energy Phys. 08 (2008) 105.
[26] G. Aad *et al.* (ATLAS Collaboration), arXiv:0901.0512.
[27] M. J. Dolan, D. Grellscheid, J. Jaeckel, V. V. Khoze, and P. Richardson, J. High Energy Phys. 06 (2011) 095.
[28] C. G. Lester, M. A. Parker, and M. J. White, J. High Energy Phys. 10 (2007) 051.
[29] B. C. Allanach, Comput. Phys. Commun. **143**, 305 (2002).
[30] F. E. Paige, S. D. Protopopescu, H. Baer, and X. Tata, arXiv:hep-ph/0312045.
[31] J. Skilling, in *Nested Sampling*, edited by R. Fischer, R. Preuss, and U. V. Toussaint, AIP Conf. Proc. No. 735 (AIP, New York, 2004).
[32] F. Feroz and M. P. Hobson, Mon. Not. R. Astron. Soc. **384**, 449 (2008).
[33] F. Feroz, M. P. Hobson, and M. Bridges, Mon. Not. R. Astron. Soc. **398**, 1601 (2009).
[34] R. Trotta, F. Feroz, M. P. Hobson, L. Roszkowski, and R. R. de Austri, J. High Energy Phys. 12 (2008) 024.
[35] B. C. Allanach, Phys. Lett. B **635**, 123 (2006).
[36] B. C. Allanach, K. Cranmer, C. G. Lester, and A. M. Weber, J. High Energy Phys. 08 (2007) 023.
[37] S. S. AbdusSalam, B. C. Allanach, F. Quevedo, F. Feroz, and M. Hobson, Phys. Rev. D **81**, 095012 (2010).
[38] M. Bridges, K. Cranmer, F. Feroz, M. Hobson, R. R. de Austri, and R. Trotta, J. High Energy Phys. 03 (2011) 012.
[39] F. James and M. Roos, Comput. Phys. Commun. **10**, 343 (1975).
[40] F. Feroz, K. Cranmer, M. Hobson, R. R. de Austri, and R. Trotta, J. High Energy Phys. 06 (2011) 042.
[41] S. Ambrosanio, G. D. Kribs, and S. P. Martin, Phys. Rev. D **56**, 1761 (1997).
[42] K. Nakamura *et al.* (Particle Data Group Collaboration), J. Phys. G **37**, 075021 (2010).
[43] S. Abel, M. J. Dolan, J. Jaeckel, and V. V. Khoze, J. High Energy Phys. 12 (2009) 001.
[44] T. Gherghetta, G. F. Giudice, and J. D. Wells, Nucl. Phys. **B559**, 27 (1999).
[45] K. Desch, J. Kalinowski, G. A. Moortgat-Pick, M. Nojiri, and G. Polesello, J. High Energy Phys. 02 (2004) 035.
[46] M. Gigg and P. Richardson, Eur. Phys. J. C **51**, 989 (2007).
[47] M. Bahr, S. Gieseke, M. Gigg, D. Grellscheid, K. Hamilton *et al.*, Eur. Phys. J. C **58**, 639 (2008).
[48] M. Gigg and P. Richardson, arXiv:0805.3037.
[49] W. Beenakker, R. Hopker, M. Spira, and P. M. Zerwas, Nucl. Phys. **B492**, 51 (1997).
[50] G. Aad *et al.* (ATLAS Collaboration), Report No. CERN/LHCC 99-15, 1999.
[51] P. Skands *et al.*, J. High Energy Phys. 07 (2004) 036.
[52] G. Bertone, D. G. Cerdeño, M. Fornasa, R. R. de Austri, C. Strege, and R. Trotta, J. Cosmol. Astropart. Phys. 01 (2012) 015.